

# A Pathway to Near Tissue Computing through Processing-in-CTIA Pixels for Biomedical Applications

1<sup>st</sup> Zihan Yin  
ECE

University of Wisconsin-Madison  
Madison, USA  
zyin83@wisc.edu

2<sup>nd</sup> Subhradip Chakraborty  
ECE

University of Wisconsin-Madison  
Madison, USA  
chakrabort42@wisc.edu

3<sup>rd</sup> Ankur Singh  
ECE

University of Wisconsin-Madison  
Madison, USA  
ankur.singh@wisc.edu

4<sup>th</sup> Chengwei Zhou  
ECSE

Case Western Reserve University  
Cleveland, USA  
chengwei.zhou@case.edu

5<sup>th</sup> Gourav Datta  
ECSE

Case Western Reserve University  
Cleveland, USA  
gourav.datta@case.edu

6<sup>th</sup> Akhilesh Jaiswal  
ECE

University of Wisconsin-Madison  
Madison, USA  
akhilesh.jaiswal@wisc.edu

**Abstract**—Near-tissue computing requires sensor-level processing of high-resolution images, essential for real-time biomedical diagnostics and surgical guidance. To address this need, we introduce a novel Capacitive Transimpedance Amplifier-based In-Pixel Computing (CTIA-IPC) architecture. Our design leverages CTIA pixels that are widely used for biomedical imaging owing to the inherent advantages of excellent linearity, low noise, and robust operation under low-light conditions. We augment CTIA pixels with IPC to enable precise deep learning computations including multi-channel, multi-bit convolution operations along with integrated batch normalization (BN) and Rectified Linear Unit (ReLU) functionalities in the peripheral ADC (Analog to Digital Converters). This design improves the linearity of Multiply and Accumulate (MAC) operations while enhancing computational efficiency. Leveraging 3D integration to embed pixel circuitry and weight storage, CTIA-IPC maintains pixel density comparable to standard CTIA designs. Moreover, our algorithm-circuit co-design approach enables efficient real-time diagnostics and AI-driven medical analysis. Evaluated on the EndoVis tissue dataset (1280×1024), CTIA-IPC achieves approximately 12× reduction in data bandwidth, yielding segmentation IoUs of 75.91% (parts), and 28.58% (instrument)—a minimal accuracy reduction (~1.3%–2.5%) compared to baseline methods. Achieving 1.98 GOPS throughput and 3.39 GOPS/W efficiency, our CTIA-IPC architecture offers a promising computational framework tailored specifically for biomedical near-tissue computing.

**Index Terms**—CTIA, In-Pixel Computing, Near-Tissue Imaging, 3D Integration

## I. INTRODUCTION

The field of computational imaging is rapidly evolving, driven by a significant push towards integrating advanced edge computing capabilities directly within image sensors. This paradigm shift aims to address the growing challenges related to data transmission bottlenecks, power consumption constraints, and the demand for real-time processing speeds. In particular, embedding computation within image sensors is

critical in biomedical and near-tissue computing applications, where the immediacy and precision of data processing directly correlate with patient outcomes. Furthermore, biomedical applications such as endoscopic surgery, which involves inserting a flexible tube with a camera and light (endoscope) into the body to visualize and operate on internal structures [1], [2], pose significant resource, power, and bandwidth constraints for endoscopic cameras. Traditional imaging systems, which rely heavily on off-chip data transfer and external processing, often suffer from latency, inefficiencies, and increased power overhead, significantly limiting their effectiveness in real-time medical imaging scenarios. As a result, researchers and industry professionals have progressively moved towards developing sensor-embedded computational solutions, ensuring efficient, timely, and accurate data interpretation close to the sensor.

One notable approach explored in recent computational imaging literature for computing-in-sensor is the Processing-in-Pixel (PIP) methodology [3]–[9]. These aim to reduce the latency and energy overhead for convolution operations by incorporating memory and computational units within individual pixels, thereby performing early-stage computation in-situ. However, these approaches have notable limitations, [3], [8], [9] has nonlinearity in output analog voltage which affects the scalability and bit-precision of the pixel circuit. The architectures described in [5]–[7] exhibit poor performance under low-light conditions, significantly limiting their suitability for biomedical imaging applications. Such inherent challenges limit the practical use of the designs, particularly for high-stakes medical imaging applications where linearity, and accuracy are paramount. The constraints associated with current in-pixel processing technologies therefore require exploring more robust and accurate pixel-level computational architectures.

To address these challenges, we introduce a Capacitive

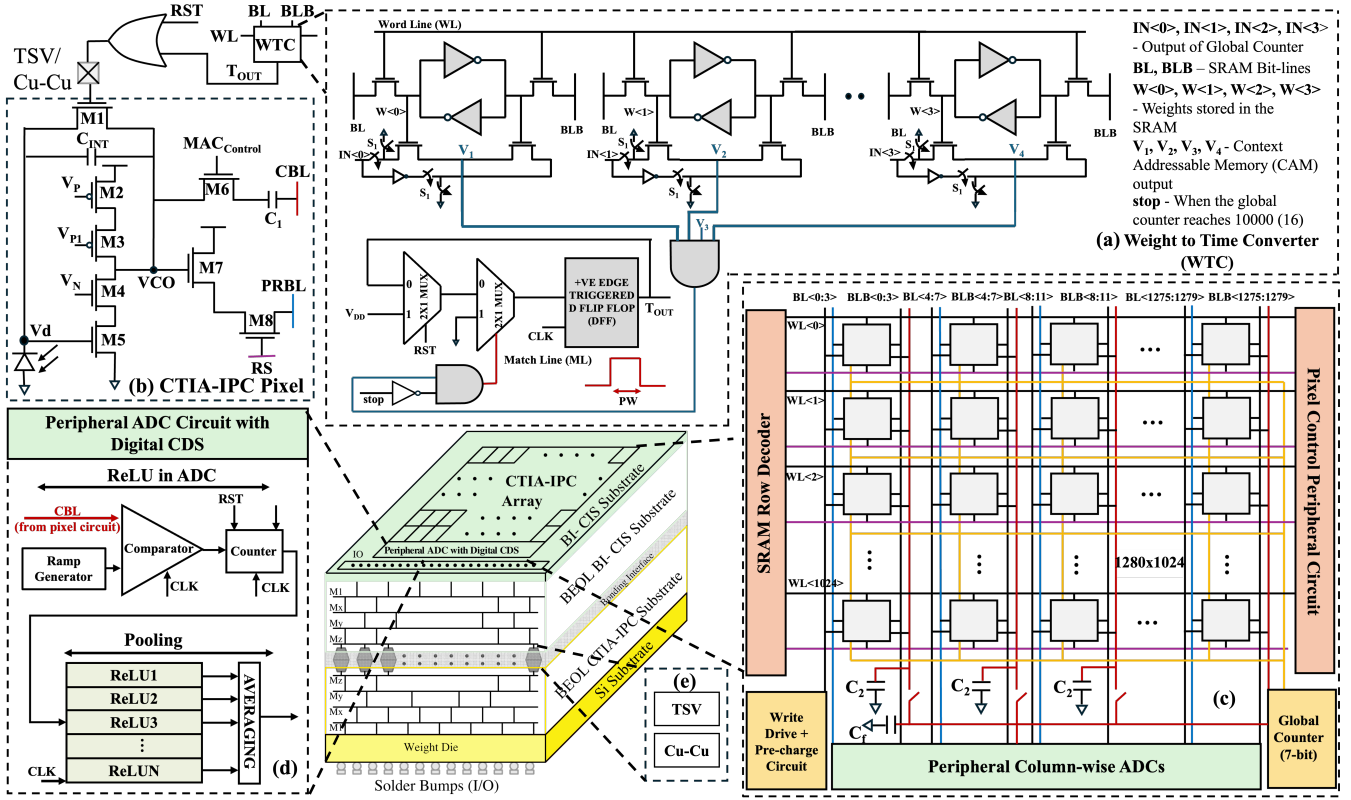


Fig. 1. CTIA-IPC architecture where (a) 4-bit Weight to time converter (WTC); (b) CTIA-IPC pixel unit circuit diagram for both multiplication and regular readout; (c) 1280×1024 CTIA-IPC Array with peripheral readout circuits; (d) Block diagram of Single Slope Analog to Digital Converter (SSADC) with Digital CDS architecture for ReLU and Pooling functionalities; (e) is the connection between the two dies using either Through-Silicon Vias (TSV) or Copper-Copper bonding (Cu-Cu) for 3D integration.

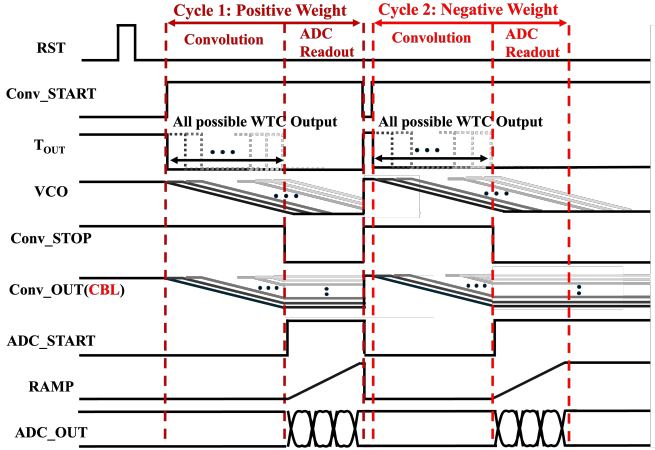


Fig. 2. A typical timing diagram for CTIA-IPC’s convolution computation showing double sampling (one for positive and one for negative weights) including Global Counter, CTIA-IPC unit and ADC’s control signals:  $RST$ ,  $Conv\_START$ ,  $Conv\_STOP$ ,  $ADC\_START$  and the output signals from these blocks:  $T_{OUT}$ ,  $VCO$ ,  $Conv\_OUT$ ,  $RAMP$  and  $ADC\_OUT$ .

Transimpedance Amplifier-based In-Pixel Computing (CTIA-IPC) architecture, leveraging the well-established CTIA pixel’s inherent linearity, low-noise characteristics, and high sensitivity under low-light conditions [10]–[12]. Building upon the advantageous properties of the CTIA pixel, our novel computational scheme CTIA-IPC integrates convolution capabilities for neural networks directly within each pixel, reducing the

reliance on external data transfers and off-chip computation.

To the best of our knowledge, this work is the first to present a CTIA-based IPC accelerator suitable for biomedical applications. The key contributions of this paper are summarized as follows:

- We propose the CTIA-IPC architecture, which supports both high-resolution conventional pixel readout operations and integrated in-pixel convolution processing.
- We implement batch normalization (BN) and Rectified Linear Unit (ReLU) activation functionality within the peripheral ADC circuit, enabling direct on-chip Convolution Neural Network (CNN) processing essential for practical biomedical imaging scenarios.
- We introduce a novel weight-to-time converter (WTC) that maps neural network weights to different exposure times, allowing the pixel to perform multiplication of input and weight for convolution efficiently.
- Applying 3D integration techniques, neural network weights are densely stored within vertically integrated SRAM cells through TSV/Cu-Cu bonding, allowing the CTIA-IPC architecture to maintain pixel-area density comparable to conventional CTIA pixel designs without incurring additional area overhead.
- By embedding robust convolution operations directly at the pixel level, our design achieves a 12× reduction in bandwidth, a computational throughput of 1.98 GOPS,

and an energy efficiency of 3.39 GOPS/W, while maintaining comparable power consumption to conventional CTIA-based pixel designs that lack computation capabilities.

- Furthermore, our algorithm-hardware co-design framework, incorporating 4-bit quantization and linearity-aware training, ensures robust segmentation performance under analog-domain constraints. It achieves competitive accuracy on the EndoVis dataset, with a minor performance drop of  $\sim 1.3\%$ – $2.5\%$  compared to baselines.

For this paper, Section II discusses the CTIA-IPC architecture in detail, Section III talks about the medical dataset we tested with the hardware, Section IV elaborates on the simulation results of the purposed circuit and Section V concludes and provides some key discussions of the paper.

## II. PROPOSED CTIA PIXEL ARCHITECTURE FOR IN-PIXEL COMPUTING

Commercial smartphone cameras are based on 3 or 4 transistor active pixel sensors [13], [14], while these pixels provide high fill factor they perform poorly in low light conditions and exhibit poor linearity. As such, these pixels are unsuitable for scientific applications. Owing to their high linearity and excellent low-light performance, CTIA pixel-based cameras are widely used for scientific applications including biomedical applications [15], [16]. In the following sub-sections we present augmenting CTIA pixels with in-situ compute capabilities targeted towards biomedical deep learning applications.

### A. Proposed CTIA-IPC Design

1) *CTIA-IPC Pixel Circuit Design*: Fig. 1(b) illustrates the CTIA pixel circuit, wherein the photodiode is held at a constant bias voltage. The circuit employs an operational transconductance amplifier (OTA)—implemented as a single-ended cascade common-source amplifier—with a gain of approximately 80 dB and a gain-bandwidth product (GBW) of 100 MHz. The OTA’s bias voltages are generated off-chip and distributed uniformly across the array. During the reset phase, the OTA output node  $V_{CO}$  is set to a reset voltage ( $V_{RST}$ ) which corresponds to the bias voltage of the OTA input transistor. Upon deactivation of the M1 nMOS reset switch, a negative charge is injected into the Vd integration node, resulting in an immediate positive jump in  $V_{CO}$ . Importantly, the diode current is defined as negative because the subsequent negative slope of  $V_{CO}$  during integration indicates a net discharge of the integration capacitor. At the end of the integration period, node  $V_{CO}$  holds the integration charge which could go through either CBL for MAC purpose or through PRBL for regular CTIA pixel readout. This is achieved by pulling up either line  $MAC_{CONTROL}$  (for MAC) or line  $RS$  (for regular readout).

2) *Weight-Time Converter (WTC)*: Neural network weights in our design are stored within SRAM cells that are vertically integrated using 3D integration techniques as shown in Fig. 1(e), enabling dense storage without incurring additional

pixel area overhead. To facilitate IPC, these SRAM cells are reconfigured as content-addressable memory (CAM) units [17] capable of performing rapid matching operations. Specifically, the WTC, depicted in Fig. 1(a), utilizes four CAM blocks that compare stored 4-bit SRAM weights against a multi-bit global counter value. The CAM cells adopt an 8T SRAM-based architecture to enable efficient in-memory XNOR operations. During write operations, switch  $S_1$  is activated, allowing standard weight storage into conventional 6T SRAM cells. For computation,  $S_1$  is deactivated to permit bitwise matching with the global counter outputs. Match signals from individual CAM blocks are combined using AND logic gate, producing a final match line that activates only when all bits align. This matched signal subsequently triggers sequential logic circuits to generate a pulse whose width accurately encodes the stored 4-bit weight. Multiplexers integrated within the sequential logic ensure proper handling of reset signals. The resolution or step size of the multi-bit global counter determines the time at which the match line goes high and in turn controls the pulse width of the time-varying signal, thereby controlling the overall precision of the WTC.

### B. CTIA In-Pixel Compute Accelerator

The CTIA in-pixel accelerator consists of a  $1280 \times 1024$  CTIA-IPC pixel array (Fig. 1(c)), with each pixel comprising a standard CTIA pixel integrated with a WTC and a capacitive charge accumulation bitline (CBL), as shown in Fig. 1(b). Each pixel operates in two distinct modes: (1) conventional high dynamic range (HDR) imaging, utilizing a standard 3T source-follower readout, and (2) an in-pixel MAC computation mode. In MAC mode, the WTC generates a 4-bit weighted timing signal ( $T_{OUT}$ ), triggering the CTIA pixel’s integration node ( $V_{CO}$ ) reset at different timestamps based on the stored weight. As illustrated in Fig. 2, signals such as  $Conv\_START$  initiate a global counter for controlling weight exposure times, while  $RST$  resets both the counter’s value and the pixel’s integration node  $V_{CO}$ ’s voltage. Unlike conventional CTIA operation, where the photodiode current results in an increase in voltage, the current in this architecture is reversed. Causing the integration voltage at node  $V_{CO}$  to decrease from  $V_{RST}$  toward 0V, rather than increasing toward  $V_{DD}$ . This design choice enhances voltage headroom and signal margin between successive MAC operations, thereby improving computational accuracy during IPC.

CNN layers typically include both positive and negative weights [18]; however, the WTC method described earlier (Section II-A2) only supports positive weights. To overcome this, we repurpose the on-chip digital correlated double-sampling (CDS) circuit commonly found in commercial CMOS Image Sensors [19]. Digital CDS is typically implemented with column-parallel single-slope ADCs (SS-ADCs), consisting of a ramp generator, comparator, and counter (Fig. 1(d)). In standard image sensor applications, CDS measures pixel reset noise and subtracts it by first counting upwards, then downwards between two samples. Leveraging this inherent up/down counting capability, our CTIA-IPC architecture

encodes positive weights through upward counting and negative weights through downward counting, accurately capturing both positive and negative contributions during pixel-level convolution. Therefore every MAC operation using CTIA-IPC requires two cycles to account for positive and negative weights. For one cycle of the CTIA-IPC MAC operation, it has two phases.

- 1) Write Phase: In the write phase, the SRAMs inside the CTIA-IPC unit are being written using a regular SRAM write-in method. At the end of the write phase, the neural network kernel weights are stored in dedicated SRAM cells which are connected to each pixel by Cu-Cu hybrid bonding.
- 2) Computation Phase: In the computation phase, all pixel columns operate in parallel. The multiplication between the stored weights using WTC and the input activation, represented by the current through the photodiode, is performed across all pixels in a column. The resulting charge accumulates on the CBL, which is shared across all pixels in a given column. At the end of each CBL, a dedicated capacitor stores the final accumulated voltage. Metal-oxide-metal (MOM) capacitors are employed due to their robustness against process variations and their ability to be integrated on top of the existing CTIA architecture, thereby minimizing area overhead. Following charge accumulation, the stored voltage is processed through a switching matrix that enables charge-domain summation across multiple columns. The configuration of the switching matrix is determined by the kernel size of the neural network being implemented. The aggregated voltage is then fed into a 6-bit CDS SS-ADC. After the SS-ADC digitizes the CBL voltage through two consecutive cycles corresponding to positive and negative weights, the quantized ReLU activation is inherently realized within the SS-ADC by clipping negative digital outputs to zero. If required by the specific algorithm, the data can then pass through an on-chip pooling layer, as illustrated in Fig. 1(d). This fully processed output is then ready to be forwarded to the subsequent neural network layers for further computation.

The ReLU operation inherently sets negative outputs to zero, aligning well with biomedical imaging applications that require precise differentiation between relevant signals and background noise. Additionally, by initializing the CDS stage with values corresponding to the scale parameters from the BN layers commonly found in convolutional neural networks, our approach facilitates direct incorporation of BN functionality. Consequently, our novel CTIA-IPC architecture efficiently integrates multi-pixel convolution computations, BN, and activation functions entirely within the pixel-level ADC circuits, effectively addressing the computational demands of critical medical imaging tasks such as rapid anomaly detection, lesion segmentation, and real-time image classification.

To achieve parallel in-situ multi-pixel convolution, for

one cycle the pixel array will activate the total number of  $\frac{(i-k+2 \times p)}{s \times lcm(k,s)} \times k^2 \times 4$  pixels simultaneously, where  $i$  denotes the spatial dimension of the input image,  $k$ ,  $p$ ,  $s$  denote the kernel size, padding and stride of the in-pixel convolutional layer, and  $\frac{(i-k+2 \times p)}{s \times lcm(k,s)}$  corresponds to the maximum number of output nodes that can be calculated at the same time,  $k^2 \times 4$  corresponds the filter size. (4 because of RGB channels). For each activated pixel, the output is modulated by the photodiode current and the SRAM. The output for each column is accumulated across the CBL followed. The CBL of these columns are then accumulated through a capacitive switching logic. A capacitive accumulation technique is employed, following the equations:

$$V_{\text{ADC\_IN}} = \frac{V_1 + V_2 + \dots + V_N}{4 + \frac{2C_2}{C_1} + \frac{C_F}{C_1}} \quad (1)$$

Where  $V_1, V_2, \dots, V_N$  are the multiplicative values generated by each CTIA-IPC unit.

### III. MEDICAL IMAGING APPLICATION

#### A. Details of the Dataset & Tasks

Minimally invasive surgery (MIS) encompasses surgical techniques that limit the size of incisions, thereby reducing wound healing time, associated pain, and risk of infection. Endoscopic surgery, a subset of MIS, involves inserting a flexible tube with a camera and light (endoscope) into the body to visualize and operate on internal structures through small incisions [1], [2]. To advance the capabilities of MIS, particularly in robotic-assisted procedures, this study focuses on surgical instrument segmentation using CNN-based models trained on a popular robot-surgery-segmentation dataset, termed *Endovis* [20]. This dataset, obtained from implantable image sensors, is well-suited for near-tissue computing, where power efficiency is crucial due to the stringent power constraints of implantable devices. In-pixel computation enabled by the CTIA-based approach is ideal for such low-power environments, as it allows feature extraction directly in the pixels, minimizing the computational load. Furthermore, the dataset's high-contrast regions and illumination artifacts demand stable early-stage feature extraction, which the linearity provided by CTIA-based in-pixel computing ensures. This preserves critical spatial details, enhancing segmentation accuracy and robustness to lighting variations and occlusions.

The dataset consists of  $8 \times 225$  high-resolution endoscopic images ( $1280 \times 1024$ ) with pixel-wise annotations for surgical instruments. The dataset is valuable for evaluating segmentation performance in robotic-assisted surgery, with three progressively challenging subtasks: binary segmentation, parts segmentation, and instrument segmentation. These tasks involve segmenting surgical tools from complex backgrounds with occlusions, specular reflections, and fine structural details.

#### B. Algorithm-Hardware Co-Design

The CTIA-IPC circuit, described in Section II, implements analog convolution using non-linear transistors in modified memory-embedded pixels. Unlike prior works that ignore

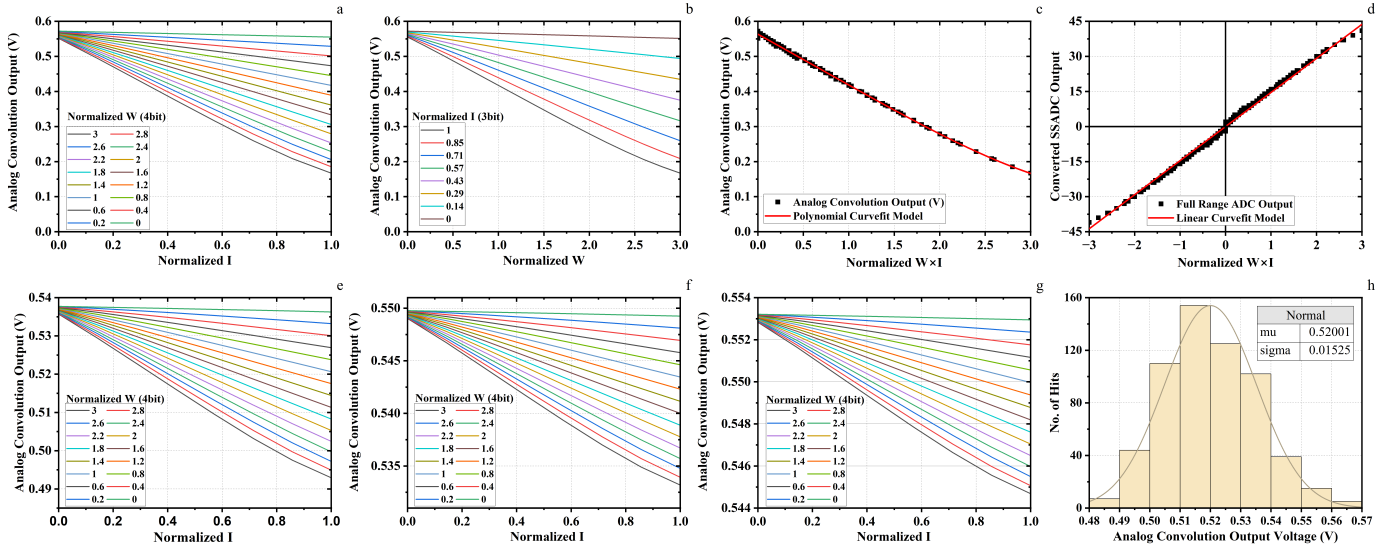


Fig. 3. CTIA circuit simulation results where (a) and (b) are the analog convolution output v.s. normalized weight  $W$  and input current  $I$  (representing light intensity), in (a) each line corresponds to different digital weight values that are translated from the WTC in the unit CTIA-IPC and in (b) each line corresponds to a specific value of input current. Scatter plots (c) and (d) shows linear curvefit function of the Convolution output value v.s. normalized  $W \times I$ , where in (c) the convolution output data is analog voltage from line CBL shown in Fig. 1(b) and in (d) is the converted digital SSADC output value. (e), (f) and (g) are the analog convolution output data v.s. sweeping one unit IPC's input  $I$  and  $W$ , where in (e) there are total of  $3 \times 3$  unit pixels, in (f)  $5 \times 5$  units and in (g)  $7 \times 7$  units. And (h) is the bar plot of monte carlo simulation result of the analog convolution output voltage.

transistor non-idealities [21], [22], we simulated the CTIA-IPC circuit with 22nm GlobalFoundries transistors, varying parameters like transistor width and photodiode current. The resulting SPICE outputs were modeled with a curve-fitting function as shown in Fig. 3(c), which replaces the convolution operation in the first network layer, similar to [3], [23]. We accumulate the function's output for each pixel in the receptive field (147 for a  $7 \times 7$  kernel with 3 input channels) to model the in-pixel convolution inner-product. To compensate for analog variations, we followed this custom convolution layer with a BN layer, then applied a ReLU operation. The ReLU output is quantized to 4 bits to reduce CTIA pixel bandwidth and is transmitted off-chip for processing the remaining layers. The BN layer is fused with the preceding convolution and succeeding ReLU layers. Consider a BN layer with trainable parameters  $\gamma$ ,  $\beta$ , and running mean and variance  $\mu$ ,  $\sigma$ . This BN layer implements a linear function during inference:

$$Y = \gamma \frac{X - \mu}{\sqrt{\sigma^2 + \epsilon}} + \beta = \left( \frac{\gamma}{\sqrt{\sigma^2 + \epsilon}} \right) X + \left( \beta - \frac{\gamma\mu}{\sqrt{\sigma^2 + \epsilon}} \right) \quad (2)$$

We fuse the scale term  $A = \frac{\gamma}{\sqrt{\sigma^2 + \epsilon}}$  into the convolutional layer weights, adjusting the pixel weight tensor to  $A \cdot \theta$ , where  $\theta$  is the trained weight tensor. Additionally, we shift the analog comparator trip point by  $B = \left( \beta - \frac{\gamma\mu}{\sqrt{\sigma^2 + \epsilon}} \right)$ , so the ReLU activation threshold becomes  $-B$ . This framework was used to optimize CNN training on the Endovis dataset.

Our algorithm builds upon TernaNet [24] through hardware-algorithm co-design, replacing the VGG11 [25] encoder's initial convolution layer (with a  $3 \times 3$  kernel, stride 1, and 64 channels) with the custom CTIA convolution module ( $7 \times 7$  kernel, stride 2, and 16 channels), and adding a batch

normalization layer as described. By omitting the subsequent max-pooling layer used in TernaNet [24], we preserve fine structural downsampling details. We train our custom TernaNet network using the Adam [26] optimizer with an initial learning rate of  $1e-4$ , trained for 20 epochs on center-cropped images. The learning rate is decayed to  $1e-5$  after 10 epochs. For binary segmentation, all instrument classes are merged into a single foreground mask, optimized using Jaccard loss. For parts segmentation and instrument segmentation, a weighted cross-entropy loss is applied additionally.

#### IV. RESULTS AND DISCUSSION

*Circuit Simulation Results:* Our modified CTIA pixel circuit is capable of performing MAC operations within a CNN layer while exhibiting improved linearity compared to existing 3T-based in-pixel computing architectures. The SPECTRE simulation results, obtained using 22nm GlobalFoundries FD-SOI technology, demonstrate that the MAC operation is a function of the weights stored in the SRAMs and the input photocurrent from the photodiode. Fig. 3(a)-(c) represents the analog convolution output voltage on line CBL to show the simulated linearity performance of the MAC operation across a range of shared input photocurrents and SRAM-stored weights. Specifically, as demonstrated in Fig. 3(c), the CTIA-based architecture achieves highly linear output responses. Fig. 3(d) illustrates the simulated digital output of the full-range SSADC, clearly demonstrating the high linearity performance of the proposed CTIA-IPC circuit. The enhanced linearity in our design is primarily attributed to the integration of an OTA within the pixel circuit and the utilization of a capacitive readout-based MAC circuit, which enables charge-based computing

System Overview	Technical Details		CNN Support					Performance Metrics	
Works	Supported Func.	Tech Node	Weight Form	Reconfigurability	BN	ReLU	Conv Linearity	Power/Pixel(W)	Efficiency (OPS/W)
APS-P <sup>2</sup> M [3]	Conv, BN, ReLU	22nm	Analog	Low	Yes	Yes	Low	0.18 $\mu$	0.4T
Reconfig [4]	Conv	180nm	Digital	High	No	No	High	0.025 $\mu$ -0.11 $\mu$	1.41-3.37T
DROIC [10]	Low Light	180nm	-	-	-	-	-	0.71 $\mu$	-
CTIA-CDS [12]	Low Light	350nm	-	-	-	-	-	3.85 $\mu$	-
CTIA-IPC (ours)	Low Light, Conv, BN, ReLU	22nm	Digital	High	Yes	Yes	High	3.26 $\mu$	3.39G

TABLE I  
COMPARISON OF CTIA-IPC WITH RELATED CTIA AND PROCESSING-IN-PIXEL WORKS.

approach further enhances the signal margin compared to prior current-domain in-pixel processing implementations [3], [4], [7]. Additionally, we leverage a hardware-algorithm co-design framework to integrate the circuit linearity characteristics into the CNN training process, ensuring that the classification accuracy remains close to state-of-the-art levels for a medical dataset.

Furthermore, we investigate the impact of kernel size on MAC operation linearity. Specifically, Fig. 3(e,f,g) confirm that the proposed CTIA-IPC architecture preserves linearity across multiple kernel sizes, demonstrating its flexibility and robustness for biomedical imaging tasks involving diverse convolutional configurations.

A key aspect of our design is the use of a 7-bit global counter with variable step size. The selection of the 4-bit subset, which is fed into the WTC block to match the stored SRAM weights, is dynamically reconfigurable. This would be beneficial to adjust to different lighting conditions for the pixel array as the global counter can select different 4bit subset to feed to the WTC which in turn changes the integration time to  $1X$  (bits 3-0 are selected),  $2X$  (bits 4-1 are selected) to  $8X$  (bits 6-3). This reconfigurable counter step size provides flexibility in adapting to different light conditions while ensuring robust MAC performance.

We perform the variability analysis considering both the process and local and global mismatches over 1000 points at a fixed weight and photodiode current. Fig. 3(h) demonstrates the change of voltage in the line CBL.

*Performance Metrics:* To quantify the bandwidth reduction (BR) after the first layer obtained by the CTIA-IPC circuit, let the number of elements in the RGB input image be  $I$  ( $i^2 \times 4$ ) and in the output activation map after the pooling layer be  $O$  ( $\left(\frac{i-k+2 \times p}{s} + 1\right)^2 \times c_o$ ). Then, BR can be estimated as:  $\frac{I}{O} \times \frac{3}{4} \times \frac{12}{N_b} \times \frac{1}{p_s^2}$  where  $c_o$  denotes the number of output channels of the in-pixel convolutional layer,  $p_s$  denotes the pooling stride size and  $N_b$  denotes the output bit precision. For a  $k = 7$  kernel size with  $p = 0$ ,  $s = 2$ ,  $c_o = 16$ ,  $N_b = 4$ ,  $p_s = 2$  our CTIA-IPC array achieves a BR of 12.08 and it exhibits a 3.26  $\mu$ W power consumption per pixel. The compute signal output was sampled from the output of a 6-bit SS-ADC. This work achieves a throughput of 1.98 GOPS with an energy efficiency of 3.39 GOPS/W. Using these performance metrics, we compare our design to prior processing-in-pixel and CTIA-based architectures, as summarized in Table I. Although the reported energy efficiency appears lower compared to existing 3T and 4T-based processing-in-pixel architectures [3], [4], this result primarily arises from our targeted low light near-

Model	Task	Binary Seg		Parts Seg		Instrument Seg	
		IoU(%)	IoU(%)	Dice(%)	IoU(%)	Dice(%)	
TernausNet [24]		80.14	77.18	86.64	30.10	42.34	
CTIA-IPC 3x (ours)		78.54	75.87	85.75	29.67	41.95	
CTIA-IPC 12x (ours)		77.59	75.91	85.81	28.58	41.03	

TABLE II  
PERFORMANCE COMPARISON OF THE BASELINE AND CUSTOM TERNAUSNET NETWORK ON THE SEGMENTATION TASKS OF THE ENDOVIS DATASET.

tissue application which requires longer exposure time. For biomedical computation BR is the key metric as BR can directly affect the efficiency of the pixel circuit. Our approach employs CTIA pixels optimized specifically for low-light biomedical imaging conditions, inherently limiting throughput and energy efficiency compared to simpler pixel designs; thus, direct efficiency comparisons to earlier processing-in-pixel works are less applicable. However, when benchmarked against existing CTIA pixel architectures [10], [12], our solution achieves competitive power consumption per pixel while uniquely integrating in-pixel computing capabilities.

*Task Accuracy:* Building upon our hardware simulation results, we now quantify the accuracy implications of the CTIA-IPC architecture when applied for medical image segmentation tasks on the Endovis dataset. We evaluated CTIA-IPC with  $3 \times$  and  $12 \times$  bandwidth reduction models, where the  $3 \times$  model is derived from the  $12 \times$  by removing the first-layer max pooling.

As Table II shows, TernausNet achieves 80.14% IoU in binary segmentation, whereas CTIA-IPC  $3 \times$  attains 78.54% IoU and CTIA-IPC  $12 \times$  further reduces this to 77.59%, corresponding to a modest degradation. For parts segmentation, TernausNet reaches 77.18% IoU and 86.64% Dice; meanwhile, CTIA-IPC  $12 \times$  reaches 75.91% IoU and 85.81% Dice, retaining approximately 98.3% and 99.0% of TernausNet accuracy, respectively. Instrument segmentation is more challenging due to its reliance on fine-grained tool articulation features, with TernausNet recording 30.10% IoU and 42.34% Dice versus CTIA-IPC  $12 \times$ 's 28.58% IoU and 41.03% Dice. Note that the  $7 \times 7$  kernel-induced spatial aliasing enhances edge preservation under low-light conditions but introduces minor precision losses in fine-grained tasks like instrument segmentation. Importantly, the  $2 \times 2$  striding in the CTIA convolution module, followed by 4-bit activation quantization and max pooling layer, reduces memory bandwidth by  $12 \times$ . This reduction is critical for real-time processing of  $1280 \times 1024$  endoscopic video, while the resulting accuracy loss is limited to 1.3%–2.5% IoU degradation, with even lower losses observed in the most challenging instrument segmentation task.



## V. CONCLUSION

In this paper, we presented a novel CTIA-IPC architecture that incorporates multi-channel, multi-bit convolution operations alongside batch normalization and quantized ReLU activation, all embedded within the pixel array and the peripheral ADC circuits. Moreover, 3D integration allow our design to store convolutional weights densely within SRAM cells at pixel level without incurring additional area overhead. The algorithm-hardware co-design strategy we adopted, including linearity-aware training and 4-bit quantization, demonstrated strong segmentation performance on the EndoVis dataset, achieving IoU scores close to baseline methods with a subtle accuracy drop ( $\sim 1.3\%$ – $2.5\%$ ). Furthermore, our design substantially reduced data bandwidth ( $12\times$  reduction), attaining a throughput of 1.98 GOPS and an energy efficiency of 3.39 GOPS/W.

Overall, the CTIA-IPC architecture provides an effective solution for accurate, real-time near-tissue computing, particularly addressing critical medical imaging requirements for high linearity and low-light sensitivity, essential in surgical and diagnostic contexts.

## REFERENCES

- [1] M. Clinic, "Minimally invasive surgery," *Mayo Clinic*, 2023.
- [2] C. Clinic, "Minimally invasive surgery: What it is, types, benefits & risks," *Cleveland Clinic*, 2023.
- [3] G. Datta, S. Kundu, Z. Yin, J. Lakkireddy, R. Mathai, A. Jacob, P. Beerel, and A. Jaiswal, "A processing-in-pixel-in-memory paradigm for resource-constrained tinyml applications," *Scientific Reports*, vol. 12, no. 1, p. 14396, 2022.
- [4] R. Song, K. Huang, Z. Wang, and H. Shen, "A reconfigurable convolution-in-pixel cmos image sensor architecture," *IEEE Transactions on Circuits and Systems for Video Technology*, vol. 32, no. 10, pp. 7212–7225, 2022.
- [5] L. Bose *et al.*, "Fully embedding fast convolutional networks on pixel processor arrays," in *Computer Vision - ECCV 2020 - 16th European Conference, Glasgow, UK, August 23-28, 2020, Proceedings, Part XXIX*, vol. 12374, pp. 488–503, Springer, 2020.
- [6] A. Roohi, S. Tabrizchi, M. Morsali, D. Z. Pan, and S. Angizi, "Pipsim: A behavior-level modeling tool for cnn processing-in-pixel accelerators," *IEEE Transactions on Computer-Aided Design of Integrated Circuits and Systems*, vol. 43, no. 1, pp. 141–150, 2023.
- [7] Z. Chen *et al.*, "Processing near sensor architecture in mixed-signal domain with cmos image sensor of convolutional-kernel-readout method," *IEEE Transactions on Circuits and Systems I: Regular Papers*, vol. 67, no. 2, pp. 389–400, 2020.
- [8] G. Datta, Z. Yin, A. P. Jacob, A. R. Jaiswal, and P. A. Beerel, "Towards energy-efficient hyperspectral image processing inside camera pixels," in *European Conference on Computer Vision*, pp. 303–316, Springer, 2022.
- [9] Z. Yin, G. Datta, M. Abdullah-Al Kaiser, P. Beerel, A. Jacob, and A. Jaiswal, "Design considerations for 3d heterogeneous integration driven analog processing-in-pixel for extreme-edge intelligence," in *2023 IEEE International Conference on Rebooting Computing (ICRC)*, pp. 1–5, IEEE, 2023.
- [10] Q. Zhang, H. Zhang, Z. Wang, R. Dou, L. Liu, Z. Zhang, J. Liu, N. Wu, and S. Li, "A  $20\mu\text{m}$  pixel-pitch, 60me-droic based on ctia for  $640 \times 512$  infrared focal plane array," in *2023 3rd International Conference on Electronic Information Engineering and Computer Communication (EIECC)*, pp. 209–213, IEEE, 2023.
- [11] K. Murari, R. Etienne-Cummings, N. V. Thakor, and G. Cauwenberghs, "A cmos in-pixel ctia high-sensitivity fluorescence imager," *IEEE Transactions on Biomedical Circuits and Systems*, vol. 5, no. 5, pp. 449–458, 2011.
- [12] M. Zou, N. Chen, Y.-s. Pu, and L.-b. Yao, "A low-light-level cmos image sensor with a novel correlated double sampling based on ctia," *Microelectronics Journal*, vol. 150, p. 106262, 2024.
- [13] J. Scott-Thomas, "Trends and developments in state-of-the-art cmos image sensors," in *2023 International Image Sensor Workshop*, 2023.
- [14] H. Murakami, E. Bohannon, J. Childs, G. Gui, E. Moule, K. Hanzawa, T. Koda, C. Takano, T. Shimizu, Y. Takizawa, *et al.*, "A 4.9 mpixel programmable-resolution multi-purpose cmos image sensor for computer vision," in *2022 IEEE International Solid-State Circuits Conference (ISSCC)*, vol. 65, pp. 104–106, IEEE, 2022.
- [15] Y. Jiang, H. Yu, X. Fu, C. Hettiarachchi, H. Xu, Y. Li, T. H. Nguyen, L. Dong, C. Dang, and Q. Zhang, "A nano-filter-integrated cmos image sensor for fluorescent biomedical imaging," in *2018 IEEE Biomedical Circuits and Systems Conference (BioCAS)*, pp. 1–4, IEEE, 2018.
- [16] D. Tran, A. Peizerat, and A. Brambilla, "A cmos readout pixel circuitry for spectral-ct applications," in *2024 19th Conference on Ph. D Research in Microelectronics and Electronics (PRIME)*, pp. 1–4, IEEE, 2024.
- [17] S. Chakraborty, D. Kushwaha, A. Bulusu, and S. Dasgupta, "An area and energy-efficient sram based time-domain compute-in-memory architecture for bnn," in *2024 IEEE 6th International Conference on AI Circuits and Systems (AICAS)*, pp. 184–188, IEEE, 2024.
- [18] A. Singh, S. Choi, G. Wang, M. Daimari, and B.-G. Lee, "Analysis and fully memristor-based reservoir computing for temporal data classification," *Neural Networks*, vol. 182, p. 106925, 2025.
- [19] K. Cho, D. Kim, and M. Song, "A low power dual cds for a column-parallel cmos image sensor," *JSTS: Journal of Semiconductor Technology and Science*, vol. 12, no. 4, pp. 388–396, 2012.
- [20] M. Allan, A. Shvets, T. Kurmann, Z. Zhang, R. Duggal, Y.-H. Su, N. Rieke, I. Laina, N. Kalavakonda, S. Bodenstedt, L. Herrera, W. Li, V. Igloukov, H. Luo, J. Yang, D. Stoyanov, L. Maier-Hein, S. Speidel, and M. Azizian, "2017 robotic instrument segmentation challenge," in *Proceedings of the IEEE Conference on Computer Vision and Pattern Recognition Workshops*, pp. 135–143, 2017.
- [21] S. Jain, A. Sengupta, K. Roy, and A. Raghunathan, "RxNN: A framework for evaluating deep neural networks on resistive crossbars," *Trans. Comp.-Aided Des. Integ. Cir. Sys.*, vol. 40, p. 326–338, feb 2021.
- [22] C. Lammie and M. R. Azghadi, "Memtorch: A simulation framework for deep memristive cross-bar architectures," in *2020 IEEE International Symposium on Circuits and Systems (ISCAS)*, vol. 1, pp. 1–5, 2020.
- [23] G. Datta, S. Kundu, Z. Yin, J. Mathai, Z. Liu, Z. Wang, M. Tian, S. Lu, R. Lakkireddy, *et al.*, "P 2 m-detrack: Processing-in-pixel-in-memory for energy-efficient and real-time multi-object detection and tracking," in *2022 IFIP/IEEE 30th International Conference on Very Large Scale Integration (VLSI-SoC)*, pp. 1–6, IEEE, 2022.
- [24] V. Igloukov and A. Shvets, "Ternausnet: U-net with VGG11 encoder pre-trained on imagenet for image segmentation," *CoRR*, vol. abs/1801.05746, 2018.
- [25] K. Simonyan and A. Zisserman, "Very deep convolutional networks for large-scale image recognition," 2015.
- [26] D. P. Kingma and J. Ba, "Adam: A method for stochastic optimization," 2017.